Low-temperature Liquid Precursors of Crystalline Metal Oxides Assisted by Heterogeneous Photocatalysis

Iñigo Bretos,* Ricardo Jiménez, Dulce Pérez-Mezcua, Norberto Salazar, Jesús Ricote, and M. Lourdes Calzada*

Dr. I. Bretos, Dr. R. Jiménez, D. Pérez-Mezcua, N. Salazar, Dr. J. Ricote, Prof. M. L. Calzada
Instituto de Ciencia de Materiales de Madrid (ICMM), Consejo Superior de Investigaciones Científicas (CSIC), Sor Juana Inés de la Cruz 3, Cantoblanco, Madrid, 28049, Spain
E-mail: ibretos@icmm.csic.es, lcalzada@icmm.csic.es
N. Salazar
Interdisciplinary Nanoscience Center, 8000 Aarhus, Denmark (present address)

Fabrication of high-performance, metal-oxide thin films requires high annealing temperatures that limit their integration in emerging technologies for large-area, flexible electronics on plastic substrates. Amorphous oxide semiconductors have recently shown processing temperatures compatible with polymeric substrates (<400 ºC),[1,2] but this remains elusive for metal oxides whose functionality relies on long-range crystalline order. Here, we report an innovative synthesis strategy for the low-temperature processing of metal-oxide layers based on the photocatalytically-assisted decomposition at room temperature of liquid precursors incorporating TiO_2 particles. The photocatalytic effect induced by TiO_2 particles upon light absorption causes a modification on the molecular structure of the precursor, promoting the partial decomposition of organics and polycondensation among the metal reagents. We demonstrate this concept on the complex oxide modeled by the ferroelectric $Pb(Zr,Ti)O_3$ perovskite, achieving crystalline thin films of adequate functionality at only 350 ºC. This facile, low-cost solution method may be transferable to any family of metal oxides, as additionally shown by the preparation of $BiFeO_3$ multiferroic thin films at 300 ºC, an exceptionally low temperature of formation for this perovskite oxide.

Metal oxides represent an outstanding class of materials whose functionality extends from electrical to magnetic to optical where they find room for diverse applications in the areas of

1

material science, chemistry, or physics. Over the past four decades, the integration of metal oxides into layers of active and passive components has constituted the basis of the technology referred to as thin-film electronics.[3] The development of different deposition techniques has enabled today a broad spectrum of physical and chemical methods to produce high-purity, high-performance thin-film materials.[4,5] In the last methods, the general process starts with the preparation of suitable *precursors*, compounds that (may) participate in chemical reactions leading to the final compound of interest after treatment; the metal oxide in its proper phase. Although precursor molecules can be rather simple, with the central metal atom bonded to species such as hydride, halide or small organic radicals, they often consist in more complex metalorganic compounds involving larger functional groups (e.g., alkoxides, diketonates, carboxylate salts).[6-8] The conversion of these precursors into the oxide phase usually proceeds via pyrolysis, whereby the organic matrix is decomposed leaving the metal cations and oxygen as a residue. To secure the optimum performance of the material, a last crystallization step can be required by annealing the oxide film at higher temperatures. During the last years, an increasing interest in the low-temperature processing of metal-oxide layers has emerged that can be related to the ever evolving development of flexible electronics.[9] This appealing technology involves the fabrication of large-area electronic devices (e.g., visual displays, solar cells, e-skin or batteries) on flexible substrates based on plastic, rubber or even paper.[10-12] The relatively low thermal stability of these supporting materials (<400 ºC), several hundreds of degrees below rigid Si wafers, compromises the maximum temperature at which the deposited oxide layer can be annealed. Due to their advantages of scalability, low-cost, and high-throughput fabrication, solution methods are best positioned to lead the challenging integration of metal-oxide layers with large-area, flexible electronic systems.[13-19] In this context, significant efforts are currently devoted to the low-temperature processing of metal oxide semiconductors by wet chemical methods.[20-23] Thin-film transistors of binary oxides (e.g., nanocrystalline ZnO or In_2O_3) have been demonstrated

2

directly on cheap, bendable substrates using deposition temperatures below 250 ºC and showing electrical performance comparable to the dominant a-Si semiconductor.[24] For more complex systems such as those based on ternary or quaternary oxides (In_2O_3-Ga_2O_3-ZnO), high carrier mobilities and degenerate band conduction are also possible using low processing temperatures at which the amorphous state still prevails.[1,2,25] However, this behavior (unique to semiconductor oxides) is not shared by most complex oxides that require a crystalline structure to hold the expected physical properties. Such situation is clearly epitomized by perovskite oxides, where high-temperature superconductivity, colossal magnetoresistance or ferroelectricity is achieved through a common crystal unit, namely ABO_3 (where A and B stand for different metal atoms). Crystallization of these perovskite layers therefore demands the application of higher annealing temperatures that prevent their direct growth on the aforementioned flexible substrates.

Considering the former scheme of thin-film fabrication, one can assume that the formation of the crystalline oxide phase cannot proceed until the total decomposition of the precursor material is carried out. The present work has been structured around such premise by introducing a novel concept built on the field of heterogeneous photocatalysis.[26,27] The fundamentals of the photocatalytic process can be briefly summarized as follows. Irradiation of a photocatalyst (e.g., TiO_2) with (UV) light having energy equal or greater than the band gap results in the generation of electron-hole pairs, followed by their separation (e^-, h^+). Although most of these charges are rapidly recombined, some of them can migrate and reach the semiconductor surface where they chemically react with adsorbed (and nearby) organic molecules producing their decomposition. If today more than 200 species can be decomposed by TiO_2 photocatalysis, including not only organic pollutants of contaminated water but also bacteria and ever tumor cells,[28] why not apply this phenomenon to decompose the organic moieties constituent of most metal precursors used by chemical solution deposition methods?

3

We have selected two multifunctional perovskite oxides such as $Pb(Zr_{0.30}Ti_{0.70})O_3$ (hereinafter, PZT) and $BiFeO_3$ (hereinafter, BFO) to prove that this is possible. The molecular precursors used for both systems together with the synthetic routes leading the respective solutions are described in Figure S1. To these solutions, photocatalytic particles of TiO_2 were introduced obtaining a 1 wt% suspension that was illuminated at room temperature from a light source with peak maxima in the UV region (see Experimental Section). After the photocatalytic process, TiO_2 particles were separated from the solution by centrifugation (see Experimental Section) obtaining thus the photocatalyzed liquid precursor. The absence of TiO_2 nanoparticles in the liquid medium was confirmed by dynamic light scattering (Figure S2). According to experimental data from FTIR spectrometry, TGA/DTA analyses, NMR and UV/Vis absorption spectroscopy, we propose the following picture to address the effect of TiO_2 photocatalysis on the synthesized solution (**Figure 1**a). As statistical phenomenon, there is a time instant in the process where the metal precursors attach to the semiconductor surface (I) and undergo the photocatalytic reactions induced by TiO_2 upon light absorption (II). The result is the chemical breakdown of organic entities in the system by a sort of advanced oxidation process carried out at room temperature. Condensation among the metal precursors may be then enhanced leading to the partial formation of an amorphous oxide (III). Crystallization of the resulting metal oxide would be favored at a lower energy stage due to thermodynamic considerations (IV). The molecular structure of the PZT precursor described here is compared by the FTIR spectra obtained in the solution at different times of the photocatalytic process (Figure S4). Figure 1b shows the evolution of two representative absorption bands at 1734 cm^{-1} [v(C=O)] and 368 cm^{-1} [v(M–O)] with time from the values calculated by their respective integrated areas. The partial decomposition of the system is deduced from the intensity decrease of the first mode ascribed to bonded atoms and/or groups typically involved in most organic compounds. Thus, the absorption band corresponding to the v(C=O) stretching mode of acetates is compared in Figure 1c for the as-synthesized

4

solution (*initial*) and after a photocatalytic process of 1440 min (*photocatalyzed*). On the other hand, the absorption band shown in Figure 1d is assigned to the ν(M–O) stretching wavenumber of metal-oxygen bonds present in the precursor. The substantial rise in the intensity of this band after photocatalysis (see Figure 1b) accounts for the formation of a [M–O–M] network that results from the condensation among the metal alkoxides (stage III of Figure 1a). The complete spectra for both initial and photocatalyzed solutions appear depicted in Figure S5. To select the optimum times for the photocatalytic process of the PZT and BFO systems, additional thermogravimetric analysis (TGA) was performed in the respective precursors (Figures S6 and S7). Figure 1e shows their decomposition temperature as a function of time, calculated by the values from which weight loss rate remains unaltered. A significant change is observed after 1440 and 360 min of photocatalysis time for the PZT and BFO systems, respectively. The advanced oxidation process reached at these stages would account for the lower temperatures required for the complete decomposition of the metal precursors. The different time elapsed for each system (PZT or BFO) can likely be explained on the basis of their respective concentrations and complexity of the organic compounds involved in each of the systems (see Experimental Section).

Despite the high organic load of the precursor solution used in this work, with practically all compounds (reagents and solvents) sensitive to TiO_2 photocatalysis, the effectiveness of this process on the cleavage of organic groups in the precursor is demonstrated by the NMR, UV/Vis and IR spectra of **Figure 2**. Data correspond to the single Ti(IV) alkoxide compound dissolved in its parent solvent (2-propanol) before and after TiO_2 photocatalysis. Comparison between NMR spectra of either [1]H (Figure 2a) or [13]C (Figure 2b) denotes chemical alterations in the precursor structure as a result of its photocatalytic decomposition. Peak assignment corresponds to the initial precursor of titanium, with those signals of the 2-propanol compound marked with an asterisk. The larger number of peaks observed after photocatalysis reveals the presence of intermediate products generated in the solution during this process.

5

The complexity of the resulting spectra did not allow the direct elucidation of their structures (out of the scope of this manuscript). However, the higher values obtained for the integrated intensities associated with the 2-propanol signals may suggest that an amount of isopropoxide ligands is released to the medium in form of alcohol after condensation of the Ti(IV) precursor. On the other hand, the absorption band at ~267 nm (Figure 2c) corresponding to the $\pi \rightarrow \pi^*$ electronic transition characteristic of acetylacetonate complexes decreases after the photocatalytic cleavage of the conjugated system existing in this metal alkoxide.[29] The release of free acetylacetone to the solution medium is evidenced by the appearance in the FTIR spectrum (Figure 2d) of a ν(C=O) stretching vibration of a ketone, which is the stable tautomer of this compound upon dissociation from the metal cation. Not only decomposition of metal precursors but also photo-oxidation of organic species can be induced by this photocatalytic process. An appreciable decrease (~45%) in the content of organic moieties associated with the gel network was calculated from EDS (energy dispersive spectroscopy) analyses performed in a xerogel layer of PZT with embedded TiO_2 particles after photocatalysis (Figure S8).

Finally, the PZT precursor of this study is evaluated in the field of the low-temperature processing of functional metal-oxide layers. Films from this liquid precursor were prepared on commercially available Pt-coated Si substrates and processed using a low-temperature fabrication scheme (see Experimental Section). **Figure 3** depicts the X-ray patterns of different samples together with the demonstration of functionality through the corresponding ferroelectric hysteresis loop and capacitance-voltage (CV) measurement. No evidence of crystallinity is observed in the diffractogram of the films deposited from the initial (non-photocatalyzed) solution after annealing at 350 ºC (Figure 3a). Only an incipient crystallization of a secondary pyrochlore phase (JCPDS 26-142) could be inferred from this pattern (~30º), whose non-ferroelectric nature leads to the linear dielectric response measured (Figure 3d).[30] On the contrary, reflections corresponding to the perovskite phase are detected

at this temperature in the films derived from the PZT precursor previously assisted by heterogeneous photocatalysis (Figure 3b). The modification of the molecular structure of this precursor, with metal atoms arranged in a manner closer to the final crystalline phase, results in the lower temperature required for its complete decomposition and crystallization of the metal oxide. The hysteresis curve of this film (Figure 3d), showing a remanent polarization of 5.5 μC cm^{-2}, supports the ferroelectric nature of the perovskite phase obtained with potential application in electronic devices.[31,32] Values between 7-10 μC cm^{-2} have been obtained in PZT films of this composition prepared on Si substrates by other techniques using annealing temperatures close to 450 ºC.[33,34] Ferroelectric domain switching is also confirmed by the two distinctive maxima observed in the corresponding CV measurement, with a value for the dielectric constant of ~70 at zero voltage and dielectric losses below 4 % (Figure 3e). To rule out any effect induced by UV light, a blank film was prepared using the same processing conditions from a precursor solution of PZT with absence of TiO_2 particles but subjected to illumination. The corresponding diffractogram (Figure 3c) confirms the crucial role of TiO_2 photocatalysis to achieve the perovskite crystallization at low temperature. The general applicability of this photocatalytically-assisted decomposition method was additionally demonstrated for the multiferroic, $BiFeO_3$ (BFO) lead-free composition. A lower limit temperature of crystallization at 325 ºC is achieved for perovskite films of this system after photocatalysis (Figure 3g), whereas those derived from the initial (non-photocatalyzed) solution remain in the amorphous state at the same processing conditions (Figure 3f). It is worth pointing that the temperature for the perovskite crystallization can even be lowered to an impressive value of 300 ºC after the application of longer soaking times (Figure S9). The topography of the BFO film was observed by scanning force microscopy (SFM) (Figure 3i), whereby inversion ferroelectric domains (180º) can be clearly discerned in the piezoresponse (PFM) mode (Figure 3j). Ferroelectricity was measured at room temperature in this film as the variation of charge current with the electric field (Figure 3k). Non-switching contributions

were subtracted from this curve by a simulation model[35] leading to the compensated loop, whose integration results in the plot of polarization versus electric field with a remanent polarization of 5.0 μC cm^{-2} (see inset). The current-voltage (I-V) curve denotes an increasing conduction close to switching voltages (Figure 3l) suggesting that the complete switching of ferroelectric domains in the film may be hampered by leakage current contribution.[36] Reduction of coercive field of this material is critical to avoid the undesired contribution of leakage currents and higher values of polarization are thus achieved for films grown by conventional methods,[36, 37] although at much higher temperatures ($\geq$500 ºC). The low processing temperature attained here led us to the direct deposition of the photocatalyzed precursor of BFO on a flexible polymeric substrate based on polyimide (see Experimental Section). The formation of the perovskite phase is corroborated by the respective X-ray pattern (Figure 3h), together with the presence of the secondary crystalline phase $Bi_2Fe_4O_9$ (JCPDS 74-1098) that is stable in this low-temperature regime (marked with an asterisk). The local piezoelectric hysteresis loops obtained, as the representative one shown in Figure 3i, confirm the ferroelectric character of this oxide prepared at only 325 ºC. This promising result supports the great technological implications of the low processing temperatures achieved in this work enabling the growth of electronic complex oxides directly on flexible substrates that cannot withstand higher temperatures, such as plastic (see Figure 3n). The presence of ferroic order in both PZT and BFO films guarantees its potential use in next-generation flexible electronics where multifunctionality provided by ferroelectric materials is expected to extend the product portfolio of this emerging platform upon integration with the semiconductor materials available today.

We believe that the photocatalytically-assisted decomposition method of metal precursors described here can constitute an enabling technology for the low-temperature processing of advanced materials using a low-cost, sustainable, and highly-versatile fabrication method. The demonstration of the concept in a complex system, such as that based on the perovskite

8

crystal unit, makes the reported strategy potentially transferable to any family of metal oxides. The multiple functionality provided by ferroelectric $Pb(Zr_{0.30}Ti_{0.70})O_3$ and multiferroic $BiFeO_3$ at processing temperatures compatible with lightweight, polymeric substrates may open the road for a wealth of applications of high-performance metal-oxide layers in the field of large-area and flexible electronics.

Experimental Section

Synthesis of Precursor Solutions and Characterization: The liquid precursor of $Pb(Zr_{0.30}Ti_{0.70})O_3$ (PZT) 0.4 M was prepared from metal reagents $Pb(CH_3CO_2)_2 \cdot 3H_2O$ (ACS reagent, ≥ 99 %, Sigma-Aldrich), $Zr(OCH_2CH_2CH_3)_4$ (70 wt% in 1-propanol, Aldrich) and $[(CH_3)_2CHO]_2Ti(C_5H_7O_2)_2$ (75 wt% in isopropanol, Aldrich), and organic solvents $CH_3CH(OH)CH_2OH$ (ACS reagent, ≥ 99.5 %, Sigma-Aldrich), CH_3CO_2H (glacial 100 %, anhydrous for analysis, Merck Chemicals) and C_2H_5OH (SeccoSolv®, max. 0.01 % H_2O, Merck Chemicals). The liquid precursor of $BiFeO_3$ (BFO) 0.125 M was synthesized by mixing $Bi(NO_3)_3 \cdot 5H_2O$ (≥ 99.99% trace metals basis, Aldrich) and $Fe(C_5H_7O_2)_3$ (≥ 99.9% trace metals basis, Aldrich) reagents in CH_3CO_2H (glacial 100 %, anhydrous for analysis, Merck Chemicals) and $HO(CH_2)_3OH$ (98 %, Aldrich) solvents. More details at Figure S1 of Supporting Information. TiO_2 particles (Degussa P25) were introduced to the former precursors in a 1 wt% concentration and dispersed with an ultrasonic cleaning bath. The suspension obtained was illuminated at room temperature for either 1440 min (PZT) or 360 min (BFO) inside a reactor equipped with a UV lamp (Ultra-Vitalux 300 W, Osram) emitting in UVA (13.6 W) and UVB (3.0 W) regions under an oxygen flow gas of 30 mLmin^{-1} and subjected to continuous stirring. The temperature in the reactor was kept below 35 ºC by a cooling system. After the photocatalytic process, TiO_2 particles were separated from the liquid precursor by centrifugation at 7000 (PZT) and 13000 (BFO) rpm for 3 min (Eppendorf 5417C). Preliminary tests on the photocatalytic efficiency of the TiO_2 particles in a non-

aqueous medium were carried out by monitoring the degradation of methyl orange in ethanol (Figure S3). Fourier-transform infrared spectroscopy (FTIR) was performed (Bruker IFS 66V-S) on gel powders derived from solutions dried at 110 ºC overnight, which were also subjected to differential thermal and thermogravimetric analyses (DTA/TGA) (Q600 TA Instruments). Aliquots from the single Ti(IV) precursor with a concentration of 0.28 M were investigated by nuclear magnetic resonance (NMR) of ^{1}H and ^{13}C nuclei (Bruker Avance III-HD Nanobay 300 MHz) with chloroform (CDCl$_3$) as deuterated solvent. Ultraviolet-visible (UV/Vis) absorption spectroscopy was also conducted (Biochrom Libra S35) in these samples diluted with deionized water down to 10^{-4} M.

Thin Film Growth and Characterization: Films from different solution precursors of PZT (0.2 M) were deposited on Pt/TiO$_2$/SiO$_2$/(100)Si substrates by dip-coating using a withdrawal speed of 150 mmmin^{-1}. Two layers were successively deposited and dried on a hot-plate at 150 ºC for 10 min. Then, the whole stack was photoannealed at 250 ºC for 1 h in oxygen (see reference [13]) and the amorphous films obtained were subsequently crystallized by rapid thermal annealing (Jipelec, JetStar 100T Processor) at 350 ºC for 5 h in oxygen, yielding a film thickness of 190 nm. For the BFO films, solutions (0.125 M) were deposited on either Pt/TiO$_2$/SiO$_2$/(100)Si or polymeric Pt/NiCr/PI substrates (see reference [19]) by spin-coating using 3000 rpm for 30 s. Eight layers were successively deposited and dried on two hot-plates at 150 ºC for 1 min and 300 ºC for 1 min. The whole stack was then crystallized by rapid thermal annealing at 325 ºC for 1 h in air, yielding a film thickness of 180 nm. X-ray diffraction (XRD) with Cu anode was used to analyze the crystallinity of the films (Bruker D8 T2T SOLX). Electrical characterization of the samples was carried out using a Radiant Precision Premier II materials analyzer. Topographies of the surfaces of the films were obtained by scanning force microscopy (SFM), using a Nanotec® Electrónica microscope controlled by WSxM® software (Nanotec Electrónica, S.L., Madrid, Spain). Piezoresponse force microscopy (PFM) images were acquired by the application of an AC voltage of 1.75 V

of amplitude at 50 kHz between the film and conductive Pt-/Ir-coated tips (PPP-NCHPt of

Nanosensors) on cantilevers with a force constant of 42 Nm^{-1}.

Supporting Information
Supporting Information is available from the Wiley Online Library or from the author.

References

[1] K. K. Banger, Y. Yamashita, K. Mori, R. L. Peterson, T. Leedham, J. Rickard, H.

Sirringhaus, *Nature Mater.* **2011**, *10*, 45.

[2] Y-H. Kim, J-S. Heo, T-H. Kim, S. Park, M-H. Yoon, J. Kim, M. S. Oh, G-R. Yi, Y-Y.

Noh, S. K. Park, *Nature* **2012**, *489*, 128.

[3] S. Ramanathan, *Thin Film Metal-Oxides: Fundamentals and Applications in Electronics*

and Energy, Springer, New-York, USA **2010**.

[4] P. M. Martin, *Handbook of Deposition Technologies for Films and Coatings*, Elsevier

Inc., Amsterdam, The Netherlands **2010**.

[5] R. W. Schwartz, T. Schneller, R. Waser, *C. R. Chim.* **2004**, *7*, 433.

[6] D. C. Bradley, *Chem. Rev.* **1989**, *89*, 1317.

[7] R. C. Mehrotra, R. Bohra, D. P. Gaur, *Metal b–Diketonates and Allied Derivatives*,

Academic Press, London, UK **1978**.

[8] U. Schubert, *J. Mater. Chem.* **2005**, *15*, 3701.

[9] A. Nathan, A. Ahnood, M. T. Cole, S. Lee, Y. Suzuki, P. Hiralal, F. Bonaccorso, T. Hasan,

L. Garcia-Gancedo, A. Dyadyusha, S. Haque, P. Andrew, S. Hofmann, J. Moultrie, D. Chu,

A. J. Flewitt, A. C. Ferrari, M. J. Kelly, J. Robertson, G. A. J. Amaratunga, W. I. Milne, *P. IEEE* **2012**, *100*, 1486.

[10] M. L. Hammock, A. Chortos, B. C.-K. Tee, J. B.-H. Tok, Z. Bao, *Adv. Mater.* **2013**, *25*, 5997.

[11] C. Wang, D. Hwang, Z. Yu, K. Takei, J. Park, T. Chen, B. Ma, A. Javey, *Nature Mater.* **2013**, *12*, 899.

[12] D. Tobjörk, R. Österbacka, *Adv. Mater.* **2011**, *23*, 1935.

[13] M. L. Calzada, I. Bretos, R. Jiménez, H. Guillon, L. Pardo, *Adv. Mater.* **2004**, *16*, 1620.

[14] P. M. Vilarinho, A. Wu, M. L. Calzada, R. Jiménez, I. Bretos (Universidade de Aveiro, CSIC) *PCT/IB2009/055699*, **2009**.

[15] A. C. Arias, J. D. MacKenzie, I. McCulloch, J. Rivnay, A. Salleo, *Chem. Rev.* **2010**, *110*, 3.

[16] C. De Dobbelaere, M. L. Calzada, R. Jiménez, J. Ricote, I. Bretos, J. Mullens, A. Hardy, M. K. Van Bael, *J. Am. Chem. Soc.* **2011**, *133*, 12922.

[17] S. Y. Chung, S. Kim, J-H. Lee, K. Kim, S-W. Kim, C-Y. Kang, S-J. Yoon, Y. S. Kim, *Adv. Mater.* **2012**, *24*, 6022.

[18] H. Kozuka, *J. Mater. Res.* **2013**, *28*, 673.

[19] I. Bretos, R. Jiménez, A. Wu, A. I. Kingon, P. M. Vilarinho, M. L. Calzada, *Adv. Mater.* **2014**, *26*, 1405.

[20] Y. Sun, J. A. Rogers, *Adv. Mater.* **2007**, *19*, 1897.

[21] S.-Y. Han, G. S. Herman, C.-H. Chang, *J. Am. Chem. Soc.* **2011**, *133*, 5166.

[22] P. F. Moonen, I. Yakimets, J. Huskens, *Adv. Mater.* **2012**, *24*, 5526.

[23] S. Jeong, J. Moon, *J. Mater. Chem.* **2012**, *22*, 1243.

[24] M-G. Kim, M. G. Kanatzidis, A. Facchetti, T. J. Marks, *Nature Mater.* **2011**, *10*, 382.

[25] K. Nomura, H. Ohta, A. Takagi, T. Kamiya, M. Hirano, H. Hosono, *Nature* **2004**, *432*, 488.

[26] A. Mills, S. Le Hunte, *J. Photoch. Photobio. A* **1997**, *108*, 1.

[27] I. P. Parkin, R. G. Palgrave, *J. Mater. Chem.* **2005**, *15*, 1689.

[28] X. Chen, S. S. Mao, *Chem. Rev.* **2007**, *107*, 2891.

[29] D. W. Barnum, *I. J. Inorg. Nucl. Chem.* **1961**, *21*, 581.

[30] G. L. Brennecka, C. M. Parish, B. A. Tuttle, L. N. Brewer, M. A. Rodriguez, *Adv. Mater.* **2008**, *20*, 1407.

[31] J. F. Scott, *Science* **2007**, *315*, 954.

[32] S-T. Han, Y. Zhou, V. A. L. Roy, *Adv. Mater.* **2013**, *25*, 5425.

[33] A. Wu, P. M. Vilarinho, I. Reaney, M. Miranda-Salvado, *Chem. Mater.* **2003**, *15*, 1147.

[34] A. Bhaskar, H. Y. Chang, T. H. Chang, S. Y. Cheng, *Nanotechnology* **2007**, *18*, 395704.

[35] R. Jiménez, C. Alemany, M. L. Calzada, A. González, J. Ricote, J. Mendiola, *Appl. Phys. A: Mater. Sci. Process.* **2002**, *75*, 607.

[36] I. Bretos, R. Jiménez, C. Gutiérrez-Lázaro, I. Montero, M. L. Calzada, *Appl. Phys. Lett.* **2014**, *104*, 092905.

[37] V. Shelke, D. Mazumdar, G. Srinivasan, A. Kumar, S. Jesse, S. Kalinin, A. Baddorf, A. Gupta, *Adv. Mater.* **2011**, *23*, 669.

Figure captions

Figure 1. Photocatalytically-assisted decomposition of a liquid precursor represented by the complex oxide Pb(Zr,Ti)O$_3$ (PZT). (a) Schemes showing different scenarios of the process, namely; (I) adsorption of metalorganic oligomers on the TiO$_2$ surface; (II) degradation of organic species by heterogeneous photocatalysis and (III) polycondensation among metal precursors and formation of an amorphous metal-oxide network at room temperature; (IV) low-temperature crystallization of the resulting precursor to the perovskite phase. (b) Peak area corresponding to FTIR bands at 1734 cm^{-1} [ν(C=O)] and 368 cm^{-1} [ν(M–O)] of the PZT precursor as a function of the photocatalysis time. (c) Comparison between FTIR bands at 1734 cm^{-1} and (d) 368 cm^{-1} of the PZT precursor after a photocatalysis time of 0 min (*initial*) and 1440 min (*photocatalyzed*). (e) Evolution of decomposition temperature of PZT and BFO precursors with photocatalysis time.

Figure 2. TiO$_2$-induced photocatalytic effects on the single Ti(IV) precursor. (a) ^{1}H and b, ^{13}C NMR spectra in the liquid Ti(IV) precursor before (*initial*) and after (*photocatalyzed*) the photocatalytic process. Assignation of peaks corresponds to the initial precursor with signals attributed to the 2-propanol parent solvent marked with an asterisk. Note that the molecular structure of this alcohol is analogous to that of the isopropoxyde ligand. (c) UV-vis spectra showing the absorption band corresponding to the π→π* electronic transition of acetylacetonate complexes. (d) FTIR spectra in the region associated with carbonyl stretching bands denoting the presence of the keto group in the photocatalyzed precursor. Inset depicts the chemical reaction of the keto-enol tautomerism.

Figure 3. Low-temperature processing of metal-oxide layers compatible with flexible polymeric substrates. (a) X-ray pattern of a PZT film processed at 350 ºC from the precursor solution as-synthesised (*initial*) and (b) after (*photocatalyzed*) the photocatalytic process. (c) X-ray pattern of a PZT film processed at 350 ºC from a precursor solution with absence of TiO$_2$ particles but subjected to the photocatalytic process described here (*blank*). (d) Ferroelectric hysteresis loops at room temperature of the PZT films derived from the initial and photocatalyzed solutions. (e) Capacitance-voltage measurement of the PZT film derived from the photocatalyzed solution. (f) X-ray pattern of a BFO film processed at 325 ºC from the precursor solution as-synthesised (*initial*) and after (*photocatalyzed*) the photocatalytic process on (g) rigid Si-based and (h) flexible polyimide (PI)-based substrates (asterisk denotes Bi$_2$Fe$_4$O$_9$ reflection). (i) Topography and (j) out-of-plane PFM phase images of the surface of the BFO film derived from the photocatalyzed solution on silicon. (k) Charge current hysteresis at room temperature of the BFO film derived from the photocatalyzed solution on silicon. Experimental (open circles), simulated (solid line), and compensated (closed squares) curves are depicted. The equivalent P vs E graph resulting from the integration of the compensated J vs E loop appears in the inset. (l) Current-voltage curve of the BFO film derived from the photocatalyzed solution on silicon. (m) Local piezoelectric hysteresis loop and (n) photograph of the flexible BFO film fabricated on polyimide with the sample size of 2x2 cm^2.
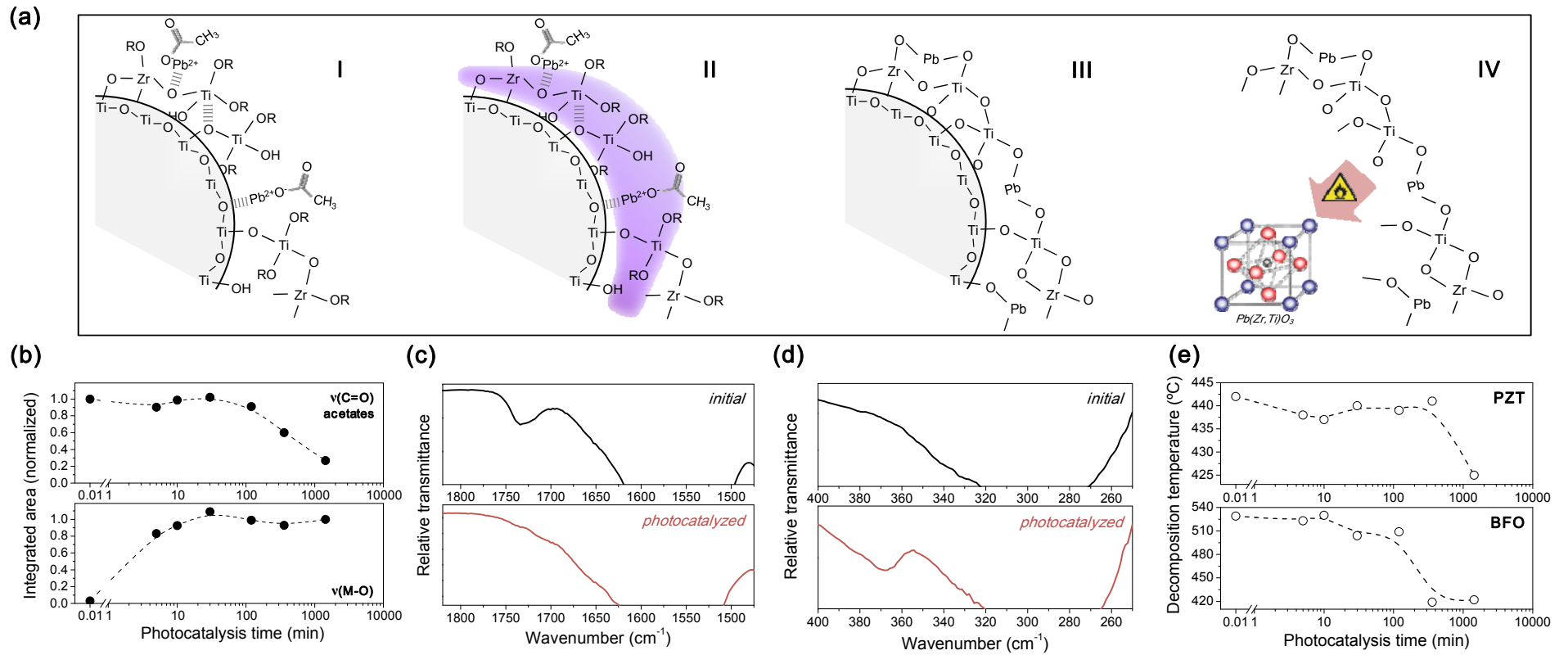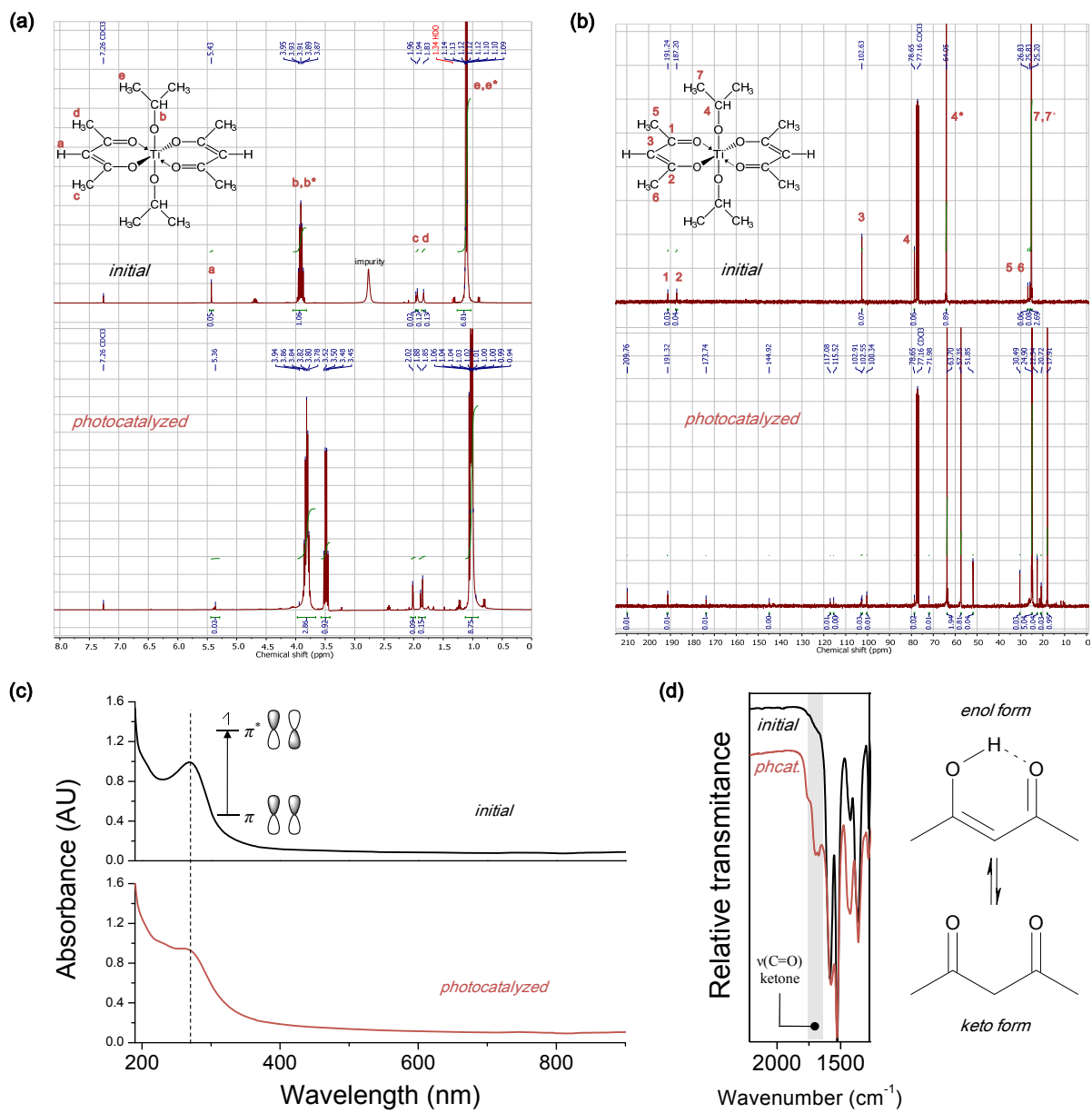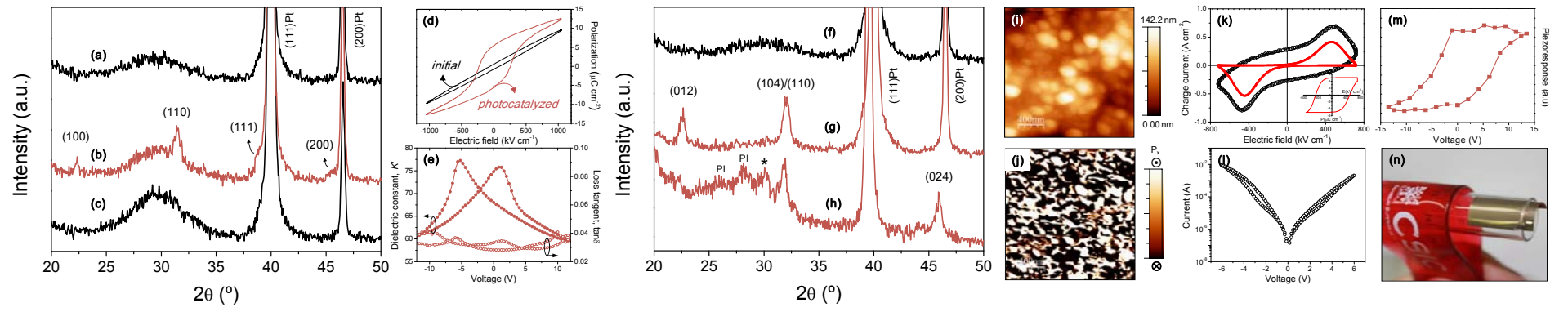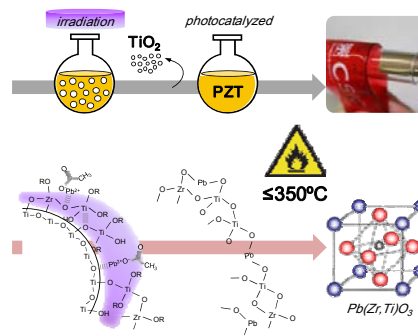
Figure 1

Figure 2

Figure 3

Low-temperature processing

I. Bretos,* R. Jiménez, D. Pérez-Mezcua, N. Salazar, J. Ricote, M. L. Calzada*

Low-temperature Liquid Precursors of Crystalline Metal Oxides Assisted by Heterogeneous Photocatalysis

The photocatalytically-assisted decomposition at room temperature of liquid precursors of metal oxides incorporating TiO_2 particles makes possible the preparation of functional layers from the ferroelectric $Pb(Zr,Ti)O_3$ and multiferroic $BiFeO_3$ perovskite systems at temperatures not exceeding 350ºC. This enables the direct deposition on flexible plastic, where the multifunctionality provided by these complex-oxide materials guarantees their potential use in next-generation flexible electronics.

Supporting Information

Low-temperature Liquid Precursors of Crystalline Metal Oxides Assisted by Heterogeneous Photocatalysis

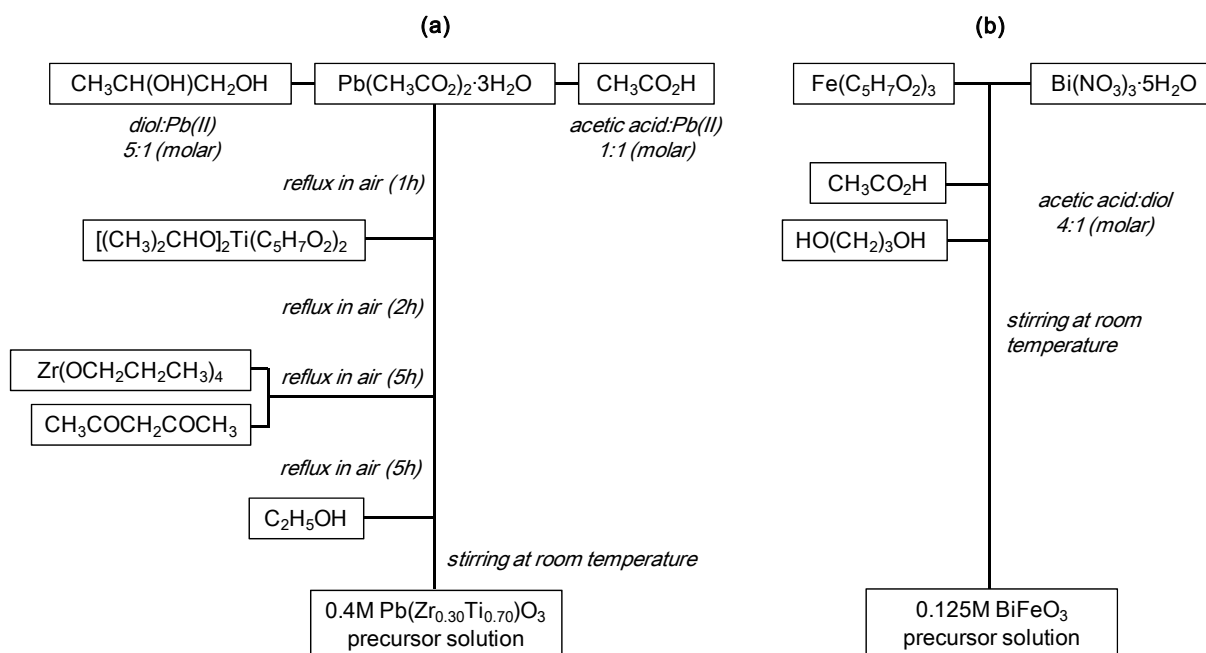*Iñigo Bretos,* Ricardo Jiménez, Dulce Pérez-Mezcua, Norberto Salazar, Jesús Ricote, and M. Lourdes Calzada**

Figure S1. Flow charts of synthetic routes leading to precursor solutions. (a) $Pb(Zr_{0.30}Ti_{0.70})O_3$ (PZT) route based on the work of Wu et al. [*J. Am. Ceram Soc.* **1998**, *81*, 2640] and modified by Calzada's group and (b) $BiFeO_3$ (BFO) original route from Gutiérrez-Lázaro et al. [*J. Am. Ceram Soc.* **2013**, *96*, 3061].
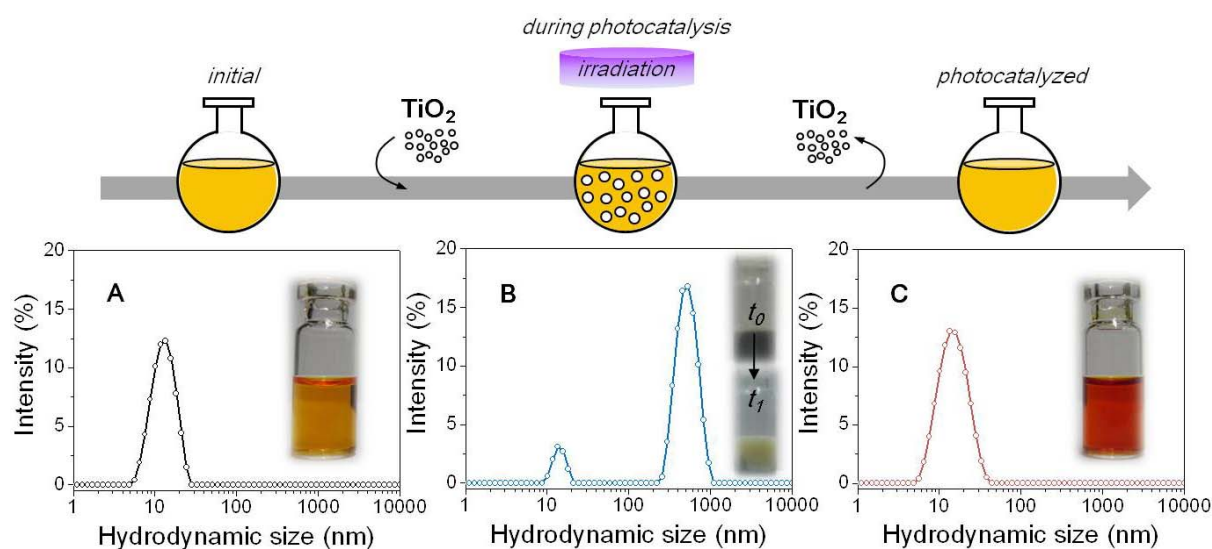
Figure S2. Particle size distributions in the Pb(Zr,Ti)O$_3$ (PZT) liquid precursor at different stages of the photocatalytically-assisted decomposition process. A Nanosizer ZS (Malvern Instrument) system was used for the measurements by dynamic light scattering (DLS). Note that the distribution of particles obtained in the initial precursor, i.e., before adding the TiO$_2$ particles, corresponds to the oligomeric species with average size ~13 nm present in the colloidal solution or sol of PZT (stage A). The presence of agglomerated TiO$_2$ particles in the suspension is evidenced by the peak maximum at average size of ~500 nm (stage B). The absence of TiO$_2$ particles in the photocatalyzed precursor after centrifugation is confirmed by the disappearance of the former peak distribution (stage C).
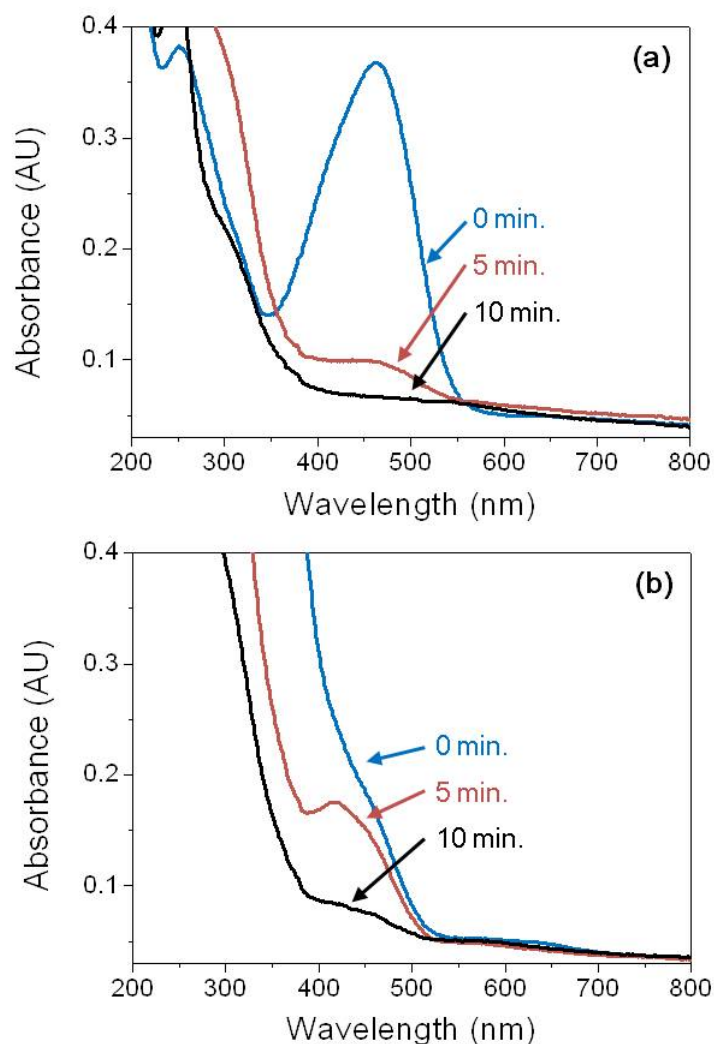
Figure S3. Photodecomposition of methyl orange using TiO_2 particles in different liquid media. (a) water and (b) ethanol. The time course of maximum absorbance at the wavelength between 420-460 nm measured by UV/Vis absorption spectroscopy (Biochrom Libra S35) corresponds to the photodegradation of methyl orange ($C_{14}H_{14}N_3NaO_3S$, MO). TiO_2 particles (Degusa P25) were added in a 0.1 wt% concentration to a MO solution (1E-4 M) and the resulting suspension was illuminated at room temperature for different times inside a reactor equipped with a UV lamp (Ultra-Vitalux 300 W, Osram) emitting in UVA (13.6 W) and UVB (3.0 W) regions under an oxygen flow gas of 30 mL min^{-1}. After the photocatalytic process, TiO_2 particles were separated from the suspension by centrifugation (Eppendorf 5417C). In spite of the higher organic content provided by the ethanol solvent, photodecomposition of MO proceeds to completion in the same time scale with respect to the aqueous solvent.
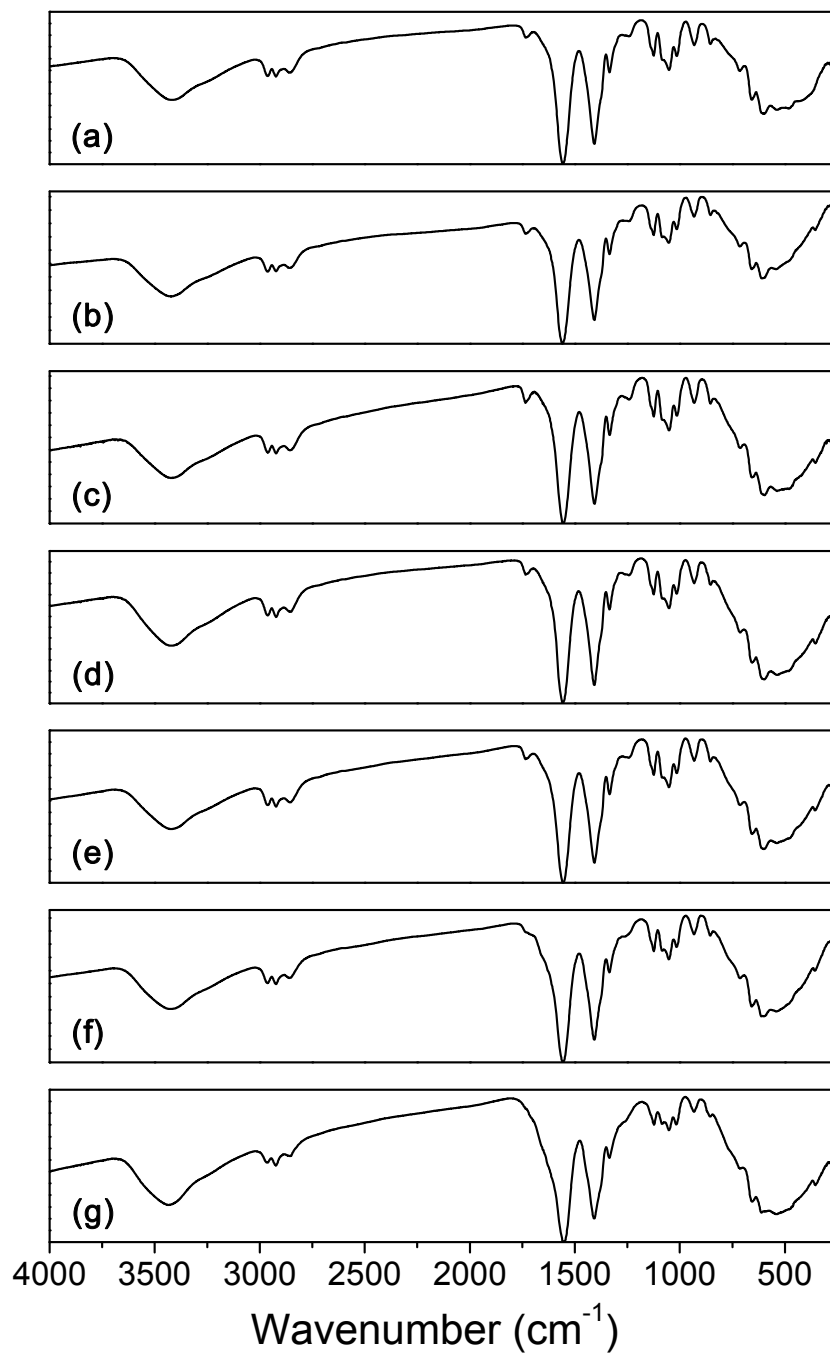
Figure S4. FTIR spectra of the PZT precursor at different times of the photocatalytic process. (a) 0 min, (b) 5 min, (c) 10 min, (d) 30 min, (e) 120 min, (f) 360 min, and (g) 1440 min.
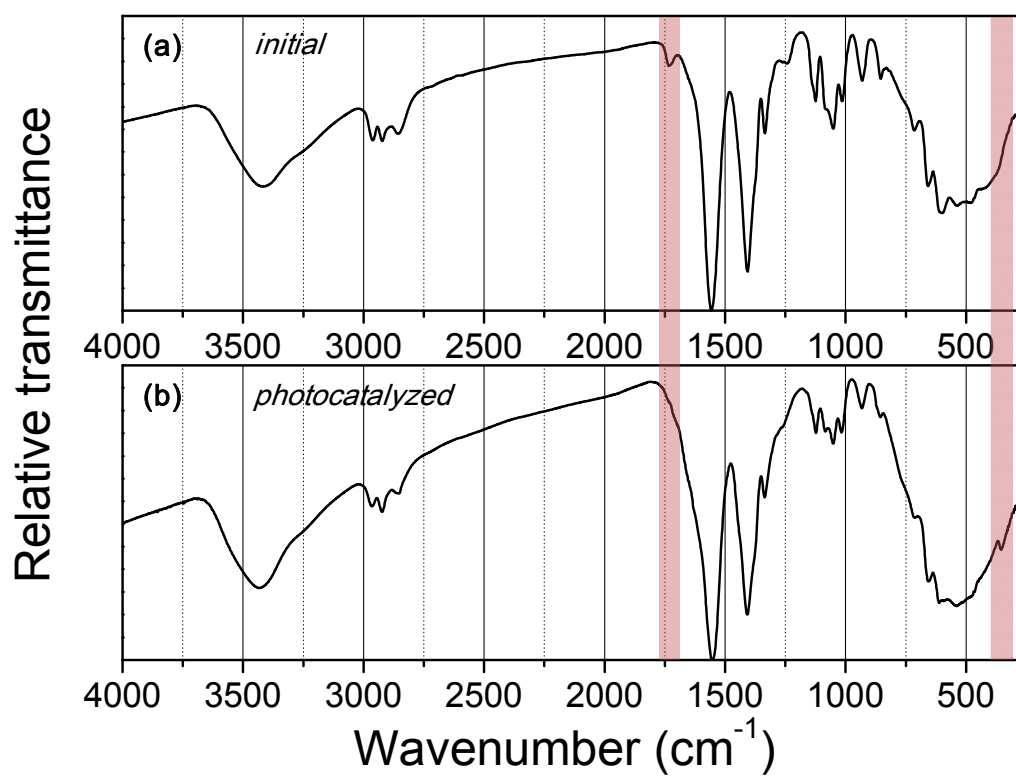
Figure S5. Comparison between the FTIR spectra of the PZT precursor at (a) 0 min (*initial*) and (b) 1440 min (*photocatalyzed*) of the photocatalytic process. Regions corresponding to vibrational modes of ν(C=O) (1734 cm^{-1}) and ν(M–O) (368 cm^{-1}) are highlighted.

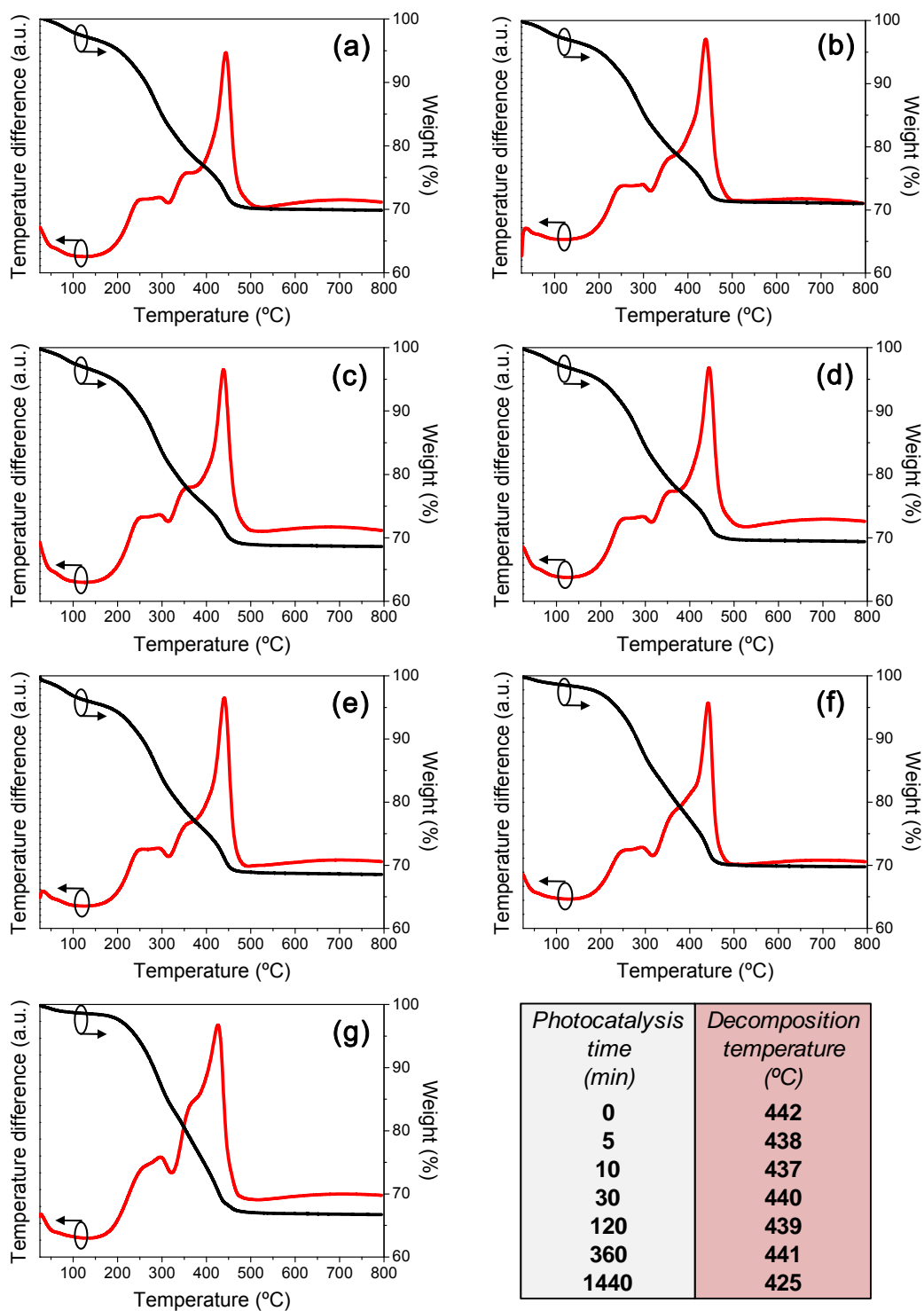| Photocalysis time (min)	Decomposition temperature (ºC)
0	442
5	438
10	437
30	440
120	439
360	441
1440	425

Figure S6. DTA and TGA curves of the PZT precursor at different times of the photocatalytic process. (a) 0 min, (b) 5 min, (c) 10 min, (d) 30 min, (e) 120 min, (f) 360 min, and (g) 1440 min. Decomposition temperatures are calculated from the respective differential TGA curves (not shown).
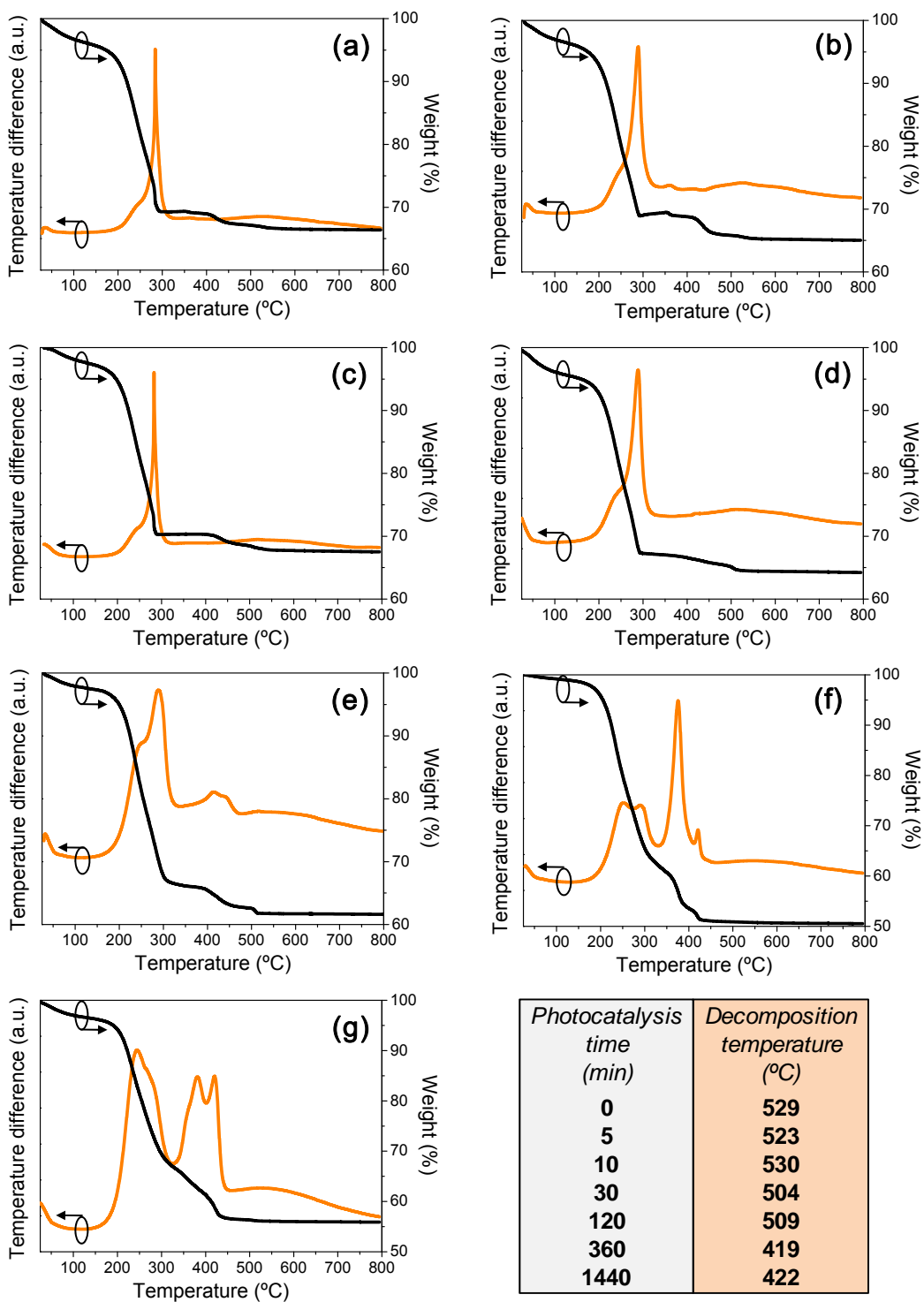
Photocatalysis time (min)	Decomposition temperature (ºC)
0	529
5	523
10	530
30	504
120	509
360	419
1440	422

Figure S7. DTA and TGA curves of the BFO precursor at different times of the photocatalytic process. (a) 0 min, (b) 5 min, (c) 10 min, (d) 30 min, (e) 120 min, (f) 360 min, and (g) 1440 min. Decomposition temperatures are calculated from the respective differential TGA curves (not shown).
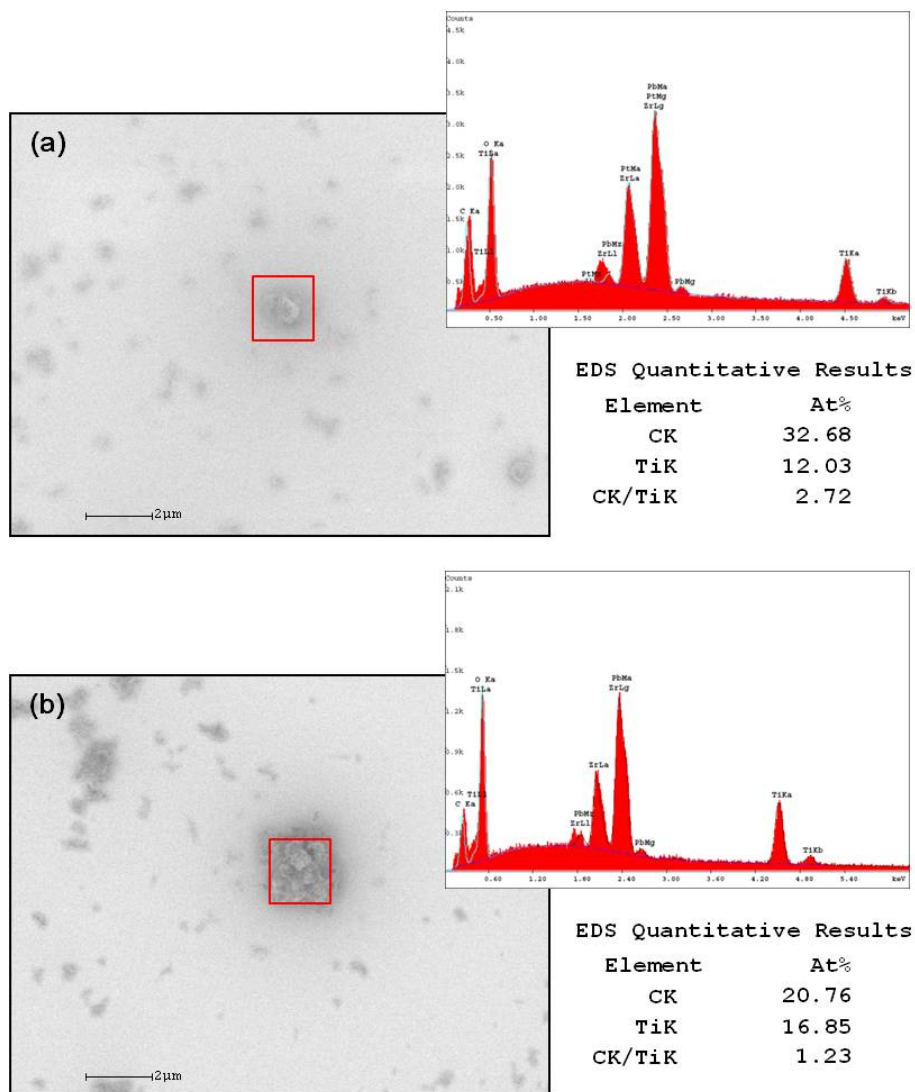
Figure S8. Photocatalytic activity in a xerogel layer derived from a suspension formed by the Pb(Zr,Ti)O$_3$ (PZT) liquid precursor with TiO$_2$ particles. (a) Surface image and EDS analysis obtained by SEM (Nova Nanosem 230 FEI Company) on a PZT film with embedded TiO$_2$ particles dried at 150 ºC and (b) subjected afterward to UV irradiation for 1 h at room temperature (Heraeus, BlueLight Excimer System, 222 nm). In general, the surface morphology reveals the presence of agglomerated TiO$_2$ particles (typically ~0.1 µm in diameter) within an homogeneous matrix of amorphous matter constituted by organic moieties associated with the inorganic gel network. To quantify the photocatalytically-assisted decomposition of organics, the relative amount of carbon surrounding a TiO$_2$ agglomerate (expressed as C to Ti ratio) was registered in identical scanned areas from both non-irradiated and irradiated regions of the sample. An appreciable decrease of ~45 % is obtained in the latter that accounts for the advanced oxidation of organic species close to the semiconductor surface upon the absorption of UV light. The possible effect derived from the size of the TiO$_2$ agglomerate selected in each region was assessed from their respective titanium concentrations measured by EDS. A difference of ~28 % is obtained that does not correlate with the relative amounts of carbon shown previously.
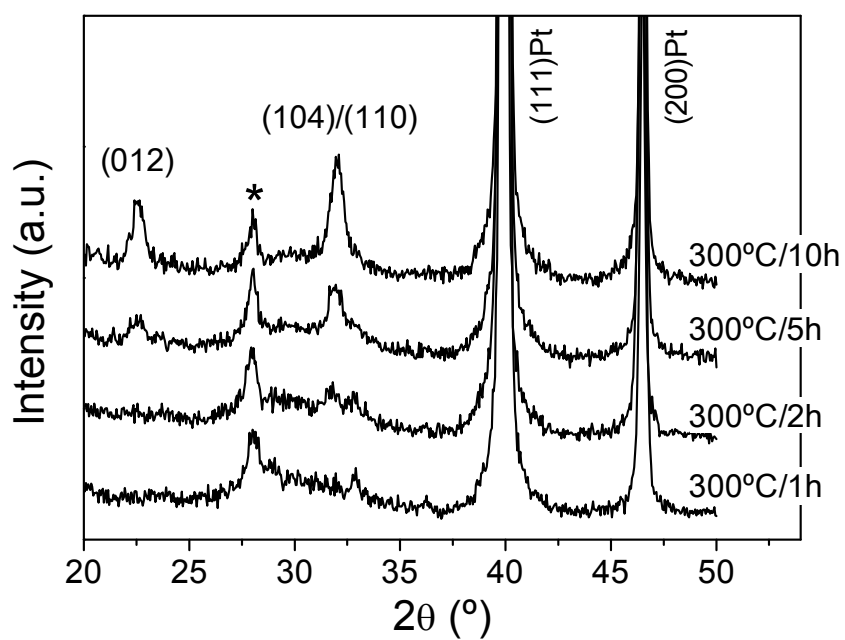
26

Figure S9. X-ray patterns of the BFO thin films prepared from the photocatalyzed solution and annealed at 300 °C for different times (asterisk denotes $Bi_{25}FeO_{40}$ secondary phase, JCPDS 46-0416).